Results in Optics 10 (2023) 100334

Contents lists available at ScienceDirect

Results in Optics

journal homepage: www.elsevier.com/locate/rio

Color optimization of a core–shell nanoparticles layer using machine learning techniques

G.M. Urquia [a], M.E. Inchaussandague [a,b,*], D.C. Skigin [a,b]

[a] Universidad de Buenos Aires, Facultad de Ciencias Exactas y Naturales, Departamento de Física, Grupo de Electromagnetismo Aplicado, Buenos Aires, Argentina
[b] CONICET - Universidad de Buenos Aires, Instituto de Física de Buenos Aires (IFIBA), Argentina

ARTICLE INFO

Keywords:
Machine learning
Optimization
Structural color

ABSTRACT

Neural networks were recently introduced in the field of nanophotonics as an alternative and powerful way to obtain the non-linear mapping between the geometry and composition of arbitrary nanophotonic structures on one hand, and their associated properties and functions on the other. Taking into account the recent advances in the application of the machine learning concept to the design of nanophotonic devices, we employ this tool for the optimization of photonic materials with specific color properties. We train a deep neural network (DNN) to solve the inverse problem, i.e., to obtain the geometrical parameters of the structure that best produce a desired reflected color. The analyzed system is a single layer of core–shell spheres composed of melanin and silica embedded in air, arranged in a hexagonal matrix. The network is trained using a dataset of the three CIE 1976 (L*a*b*) color coordinates obtained from the simulated reflectance spectra of a large set of structures. The direct problem is solved using the Korringa–Kohn–Rostoker method (KKR), widely applied to calculate the optical properties of sphere composites. The color optimization approach used in this work opens up new alternatives for the design of artificial photonic structures with tunable color effects.

1. Introduction

Deep learning (DL) is a subfield of machine learning, which allows computational models to make predictions and classifications. These models are composed of multiple processing layers inspired by the biological neural networks present in the brains of animals. DL is used in computer vision, speech recognition, image classification and pattern recognition, among other applications (LeCun et al., 2015; Goodfellow et al., 2016). In addition, this data-driven technique can be applied to problems in physics, chemistry, biology and medicine (Baldi, 2021).

Very recently, DL has emerged in the field of nanophotonics as a new approach to obtain the relationship between the geometry and composition of arbitrary nanophotonic structures, and their associated properties and functions. An advantage of the design strategies based on DNN is that, although they require a large amount of simulations to build a database, once it is completed the developed DNN can be used to optimize different structures. In contrast, conventional optimization strategies are computationally expensive because they require the iterative simulation of the response using an electromagnetic method.

Various DNN model architectures have been employed depending on the photonic tasks. For instance, they have been used for the design of photonic structures (Ma et al., 2021), to obtain approximate solutions of electromagnetic problems, such as light scattering by multilayered nanoparticles (Peurifoy et al., 2018), to characterize plasmonic nanostructures (Malkiel et al., 2018) and also for inverse design (Molesky et al., 2018; Pilozzi et al., 2018). In particular, DL has attracted the attention of different research groups as a novel alternative for inverse design of nanostructures exhibiting structural colors (González-Alcalde et al., 2018; Huang et al., 2019; Baxter et al., 2019; Sajedian et al., 2019; Dai et al., 2021).

Structural coloration involves the selective reflectance of incident light by the physical characteristics of a structure. A large variety of examples are found in nature. In particular, avian feathers exhibit a high diversity of structural colors, many of those are produced by arrays of melanosomes (solid or hollow melanin-containing organelles), such as in birds of paradise and in common bronzewings (Stavenga et al., 2015; Xiao et al., 2014). These examples inspired the design of homogeneous (Xiao et al., 2015) and of core–shell synthetic melanin nanoparticles for the production of bright structural colors (Xiao et al., 2017). The control of the shell-to-core radius ratio and the spacing between nanoparticles allows to obtain tunable colors across the entire visible spectrum.

* Corresponding author at: Universidad de Buenos Aires, Facultad de Ciencias Exactas y Naturales, Departamento de Física, Grupo de Electromagnetismo Aplicado, Buenos Aires, Argentina.
E-mail address: mei@df.uba.ar (M.E. Inchaussandague).

https://doi.org/10.1016/j.rio.2022.100334
Received 15 July 2022; Received in revised form 3 November 2022; Accepted 4 December 2022
Available online 15 December 2022

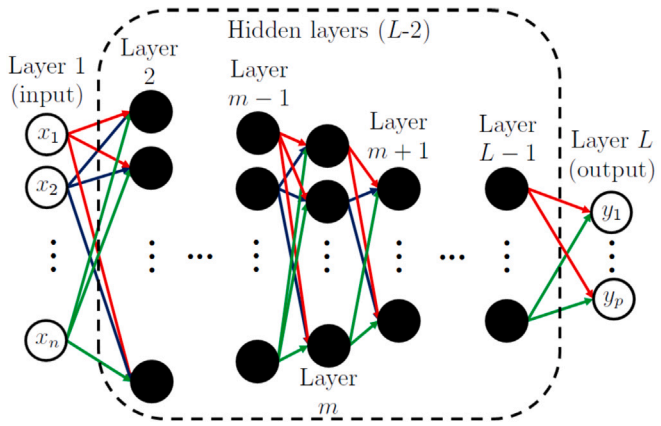

Fig. 1. Scheme of a fully connected DNN of L layers: an input layer, $L-2$ hidden layers, and an output layer.

In this contribution we apply an inverse design strategy using DNNs to obtain the geometrical parameters of a layer of spherical core–shell nanoparticles that reproduce a desired color. We focus on core–shell spheres comprising materials of high refractive index (RI) contrast. We consider melanin nanospheres (high RI and broad absorption across the visible spectrum) coated with silica (low RI) (Xiao et al., 2017).

The present paper has four sections. In Section 2 we describe the inverse design strategy used to predict the geometrical parameters of a structure that produces a given reflected color using a fully connected deep neural network. The results obtained are shown in Section 3. First, we present the color databases obtained by simulating the response of the studied structures using the program MULTEM2, a numerical implementation of the Korringa–Kohn–Rostoker method (KKR) (Stefanou et al., 1998; Yannopapas et al., 1999; Stefanou et al., 2000). Then, we describe the training, validation and testing stages of the DNN model and we illustrate its prediction capability. Finally, concluding remarks are given in Section 4.

2. Formulation of the problem: prediction of geometrical parameters

We aim to use a DNN to predict the geometrical parameters of a single layer of core–shell melanin nanoparticles (CS-MNPs) that produces a given reflected color specified by its color coordinates. For this purpose, the DNN is trained with the objective of minimizing the difference between the target and the retrieved colors.

The DNN used in this work is fully connected. Within this model (see Fig. 1), a network with L layers of neurons is composed of an input layer that receives the information provided by the input variables $(x_1, x_2, \ldots, x_n)$, $L-2$ layers (hidden layers) that perform transformations to the input data, and an output layer that retrieves the output variables $(y_1, y_2, \ldots, y_p)$.

Each neuron in a hidden layer receives information from all neurons in the previous layer, and performs a linear combination of two types of parameters called weights and biases. If there is a nonlinear mapping between the inputs and the outputs of the DNN, it is necessary to apply a nonlinear activation function (Rasamoelina et al., 2020) in the output of all neurons in each hidden layer. Thus, by incorporating nonlinearity into the DNN model, the network is able to learn complex representations. The output of the j-th neuron in the m-th hidden layer is obtained as (Ma et al., 2021):

$$a_j^m = \sigma\left(\sum_{k=1}^{N_{m-1}} w_{j,k}^m\, a_k^{m-1} + b_j^m\right), \tag{1}$$

where $w_{j,k}^m$ is the weight for the input a_k^{m-1} (coming from the k-th neuron in the $(m-1)$-th hidden layer), b_j^m is the bias of the neuron considered, N_{m-1} is the number of neurons in the $(m-1)$-th hidden layer, and $\sigma(x)$ is the activation function. The output variables (predictions) are obtained using the information that comes from the neurons of the $L-1$ hidden layer: $y_j = \sum_{k=1}^{N_{L-1}} w_{j,k}^L\, a_k^{L-1} + b_j^L$.

The weights and biases are learned by the DNN during the training stage through an iterative process, with the aim of minimizing a loss function that measures the differences between the target and the output values predicted using an optimization algorithm. In the training stage, the DNN is able to learn relationships between input and output variables in order to improve the matching between the target and the output data. At the beginning of this stage the values of the weights and the biases are initialized (in this work the weights are arbitrarily assigned and the biases are set to zero). Then, in each iteration of the process the DNN is fed by a set of samples (batch size) of a given database, the loss function is calculated, and the weights and biases are updated. Once the DNN is fed with the entire data set, an epoch is completed and the process can be repeated. Once the weights and biases are learnt and established, a DNN model is built and it can be used to make predictions.

3. Results

3.1. Color database

Our goal is to train the DNN to learn the nonlinear relationship between the relevant geometrical parameters of the CS-MNPs layer, and their corresponding three color coordinates in the CIE 1976 (L*a*b*) (CIELAB) color space. The training process employs a database, and to create it, the direct problem must be solved. In this work, this implies to obtain the color coordinates from the simulated reflectance spectra of many similar structures which share all the parameters except those selected as target variables to be optimized. The reflectance response of the system is calculated using the KKR method, which was extensively used to compute the optical properties of multilayer structures comprising homogeneous slabs and/or layers of regularly distributed spheres (Stefanou et al., 1998).

In Fig. 2 we schematize the structure considered and the incidence conditions: the CS-MNPs are located at the sites of a hexagonal Bravais lattice with lattice constant a. The whole layer is embedded in air and is normally illuminated by a linearly polarized (along the X or Y direction) plane wave of wavelength λ. Taking into account the symmetry of the problem, for normal illumination the optical response of the system is independent of the polarization mode (transverse electric or transverse magnetic). Each nanosphere has a melanin core of radius R_1 surrounded by a silica shell of thickness $R_2 - R_1$, as shown in the inset of Fig. 2. The refractive index of melanin $n_m = \eta_m + i\,k_m$ is complex and depends on the wavelength. To model the wavelength dependency of its real part we used the Cauchy formula $\eta_m = A + \frac{B}{\lambda^2}$, with $A = 1.648$ and $B = 23700$ nm^2, and for the imaginary part we considered $k_m = Ce^{-\lambda/D}$, with $C = 0.56$ and $D = 270$ nm (Stavenga et al., 2015). The refraction index of silica is 1.45.

The relevant geometrical parameters responsible for the optical response of the studied structure are R_1, R_2 and a. In this work we aim at predicting the values of R_1 and a, while R_2 is kept fixed. Therefore, to build the database, we obtain the reflectance spectra for many structures which share the same value of R_2 and differ in R_1 and a. For each of these spectra we calculate the three CIELAB color coordinates, and the whole set of these coordinates constitutes the complete database.

Since the investigated structure is a 2D regular arrangement, diffraction orders other than the specular order can arise depending on the values of λ and a. Given a Bravais lattice, a general reciprocal lattice vector can be written as $\mathbf{g} = p\,\mathbf{b}_1 + q\,\mathbf{b}_2$, where $\mathbf{b}_1$ and $\mathbf{b}_2$ are the primitive vectors in the reciprocal space and p, q are integers. For a hexagonal Bravais lattice $\mathbf{b}_1 = 4\pi\hat{y}/(\sqrt{3}a)$ and $\mathbf{b}_2 = 2\pi(\hat{y}/\sqrt{3} - \hat{x})/a$. Then, taking into account that the diffraction channels are open for $|\mathbf{g}| < 2\pi/\lambda$,

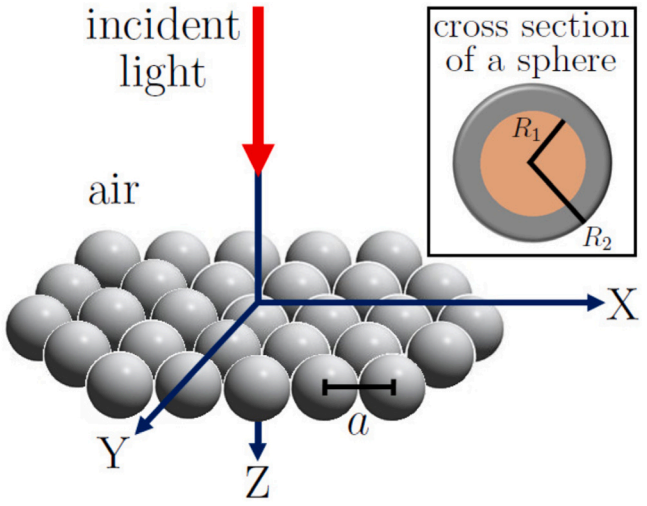

Fig. 2. Scheme of the studied structure: a single layer of spherical core–shell nanoparticles arranged in a hexagonal Bravais lattice, embedded in air. In the inset we schematize the cross section of each core–shell sphere. The relevant geometrical parameters are indicated.

we have a diffraction cutoff whenever $|\mathbf{g}| = 2\pi/\lambda$, which in this case reduces to (Dorado et al., 2008):

$$\frac{a}{\lambda} = \sqrt{p^2 + \frac{(2q+p)^2}{3}}, \tag{2}$$

where we assumed that the refraction index of the embedding medium is 1. In this work, to optimize the reflected color we focus on the specular reflectance, i.e., only the 0-th diffraction order is analyzed.

Once the specular reflectance of the whole set of structures is obtained, the color coordinates can be computed. The three standard tristimulus values X, Y and Z are calculated first (Gralak et al., 2001):

$$\begin{aligned} X &= \frac{1}{k}\int D(\lambda)\,R(\lambda)\,\overline{x}(\lambda)\,d\lambda\,, \\ Y &= \frac{1}{k}\int D(\lambda)\,R(\lambda)\,\overline{y}(\lambda)\,d\lambda\,, \\ Z &= \frac{1}{k}\int D(\lambda)\,R(\lambda)\,\overline{z}(\lambda)\,d\lambda\,, \end{aligned} \tag{3}$$

where $\overline{x}$, $\overline{y}$ and $\overline{z}$ are called color-matching functions and describe the chromatic response of the observer, $R(\lambda)$ is the reflectivity of the structure under study, $D(\lambda)$ is the energy distribution of the illuminant, and k is a normalization factor defined in such a way that an object with a uniform reflectivity $R(\lambda) = 1$ gives a luminance value $Y = 1$. To analyze the color observed by the human eye, it is sufficient to retain only the wavelengths within the visible range (380–780 nm) in the integrals of Eq. (3). We consider a standard illuminant D65 (Daylight 6500 K) that represents daylight, and a visual field of 2° (Lozano, 1978).

The tristimulus values X, Y, Z are a basis to obtain the color coordinates in different spaces. In this work we use the CIELAB color space, which was recommended in 1976 and has been extensively employed in paint, plastic and textile industries. L*, a* and b* are the color coordinates of a point in a three-dimensional color space, in which the L* axis correlates with lightness and takes values in the range 0–100, the a* axis correlates with greenness (−a*) and redness (+a*), and the b* axis represents blueness (−b*) and yellowness (+b*). These coordinates are given by the following equations (McLaren, 1976):

$$\begin{aligned} \mathrm{L}^* &= 116\left(\frac{Y}{Y_o}\right)^{1/3} - 16\,, \\ \mathrm{a}^* &= 500\left[\left(\frac{X}{X_o}\right)^{1/3} - \left(\frac{Y}{Y_o}\right)^{1/3}\right], \\ \mathrm{b}^* &= 200\left[\left(\frac{Y}{Y_o}\right)^{1/3} - \left(\frac{Z}{Z_o}\right)^{1/3}\right], \end{aligned} \tag{4}$$

where X_o, Y_o, and Z_o are the corresponding tristimulus values of a perfectly reflecting diffuser illuminated by the same light source used to obtain X, Y and Z. The values of the coordinates are normalized so that $Y_o = 100$.

In Figs. 3(a)–(d), we present the specularly reflected color palette obtained for regular structures formed by a layer of CS-MNPs, considering different values of R_2: (a) 130 nm, (b) 150 nm, (c) 170 nm, and (d) 190 nm. As stated above, in each case we consider regular structures that differ in two parameters: R_1 and a. a is varied between 301 and 799 nm in steps of 2 nm, and R_1 is varied between $0.4R_2$ and $0.99R_2$ in steps of $0.01R_2$. Notice that for each value of R_2, the range of a has been restricted to fulfill the condition of non-overlapping spheres ($a \geq 2R_2$). Therefore, while the color maps in Figs. 3(a) and 3(b) cover the colors obtained for 15000 structures, those in Figs. 3(c) and 3(d) are obtained by simulating 13800 and 12600 structures, respectively.

As mentioned above, we analyze the specular reflectance. Notice that, according to Eq. (2), for $a/\lambda < 2/\sqrt{3}$ only the 0-th diffraction order can propagate. This implies that for $a < (2/\sqrt{3})\,380$ nm ≈ 438 nm, this condition is guaranteed for all the visible wavelengths, although for $a > 438$ nm higher diffraction orders appear.

It was shown experimentally that a self assembly of core–shell nanoparticles comprising a melanin core and a silica shell, can produce tunable colors by controlling the shell thickness (Xiao et al., 2017). Here, we expand this idea and cover a wider range of variation of the geometric parameters. As observed in Fig. 3, we show that when light interacts with the layer of core–shell spheres, attractive and varied reflected colors are generated. As a increases, the color gamut ranges from the blues to the reds, including a wide variety of hues. Notice that there exist multiple structures in each color map which display similar colors. This characteristic is of relevance for the retrieval process because it implies that more than one solution (optimized structure) could be retrieved for a given target color. On the other hand, it can be noticed that for the largest values of R_2 (Figs. 3(c)–(d)), the color response seems to be more sensitive to the value of R_1 for $a < 600$ nm, approximately. Moreover, different hues that do not appear for smaller values of R_2 are obtained, as the light purple tone observed in Fig. 3(d) for $R_1/R_2 > 0.8$ and $a \approx 500$ nm.

It is useful to represent the color coordinates of the databases in the 3D CIELAB color space. This representation of the color database permits to identify the potential and limitations of the set of considered structures to produce a desired color, prior to the optimization process. In Fig. 4 we show these representations for the color coordinates of the databases of Fig. 3. As observed, complex shapes of the color space regions are identified in the four cases. These shapes are associated with the range of colors that are achievable for each value of R_2. For instance, Fig. 4(a) reveals that although the color palette shown in Fig. 3(a) seems to cover most of the visible spectrum colors, the database colors are restricted to a well defined region in the color space, meaning that only those hues contained in this region will be reachable by the optimization process. It can be noticed that as R_2 is increased, the green and yellow regions become larger, while the blue zones are reduced. In addition, the structures generated by varying the external radius can exhibit colors with different shades. For example, the points in the green region of the color space in Fig. 4(d) have higher values of the coordinate L* than the points in the green region of Fig. 4(a), which means that the displayed green colors are lighter.

In the next section we outline the procedure followed to train the DNN model, to be able to predict the optimized values of R_1 and a that produce a desired specular color. To do so, we employ the built databases represented in Figs. 3 and 4.

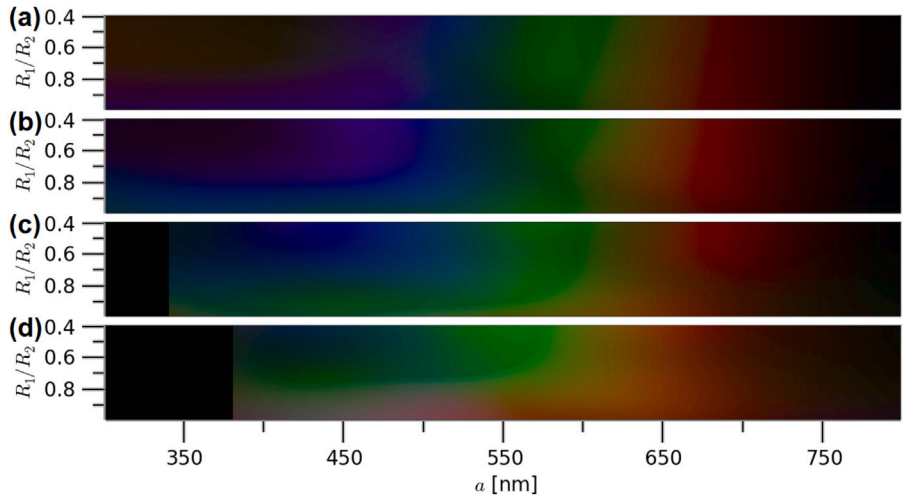

Fig. 3. Specularly reflected color of a single layer of melanin nanospheres coated with silica under normal illumination, as a function of a and R_1/R_2, for the following values of R_2: (a) 130 nm; (b) 150 nm; (c) 170 nm; (d) 190 nm.

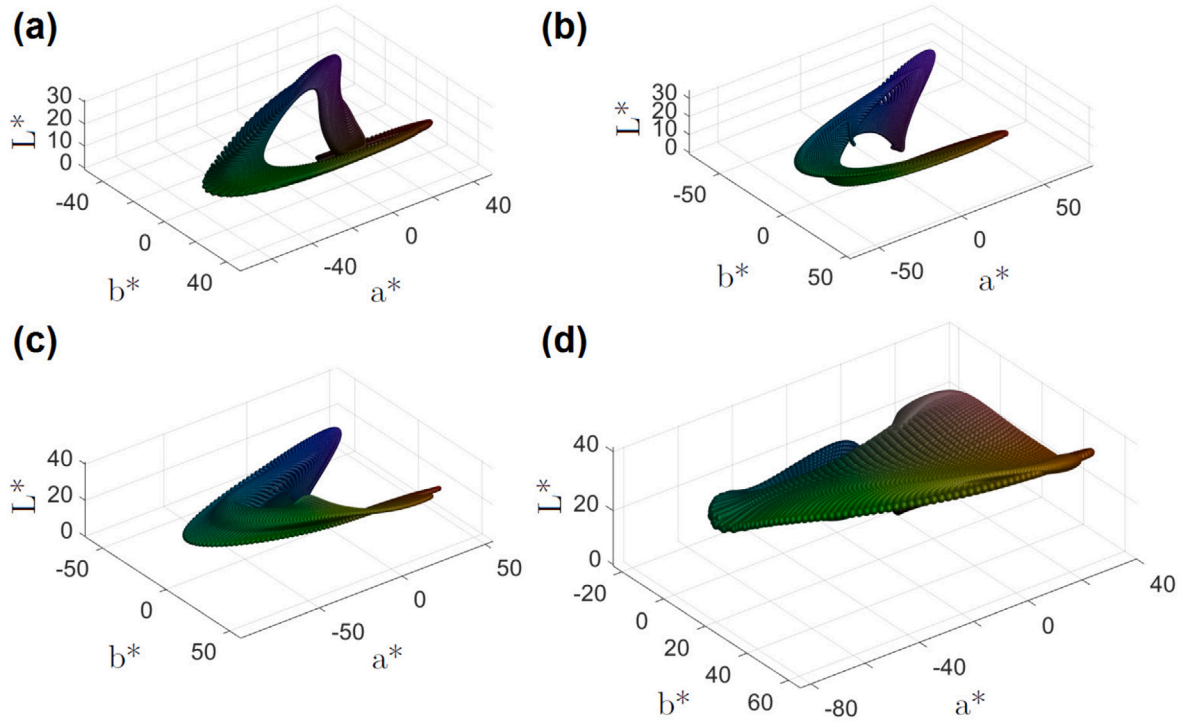

Fig. 4. Color databases shown in Fig. 3 represented in the 3D CIELAB color space. Panels (a)–(d) correspond to Figs. 3(a)–(d), respectively.

3.2. Training, validation and testing of the model

In this section we illustrate the inverse problem solution process using a fully connected DNN. Before starting the optimization process, the databases employed are split into three subsets: 80% of the available data is used to train the DNN (training data), and the remaining 20% is equally divided into validation and test data. We use the validation data to evaluate the performance of the DNN model during the training stage. This data allows us to establish how accurately a model is able to identify relationships between input and output variables, before using the DNN to make predictions. Validation data may be used to choose the features of the DNN architecture and the critical model parameters, such as the number of hidden layers and the number of neurons in each layer, the batch size and the number of epochs, the activation function and the optimization algorithm.

As usually employed in regression problems that require the prediction of quantities, the loss function minimized to update the weights and biases is the mean squared error (MSE), defined as the average of the squared differences between the target values $\hat{y}_i$ and the predictions y_i:

$$\mathrm{MSE} = \frac{1}{N}\sum_{i=1}^{N}(y_i - \hat{y}_i)^2, \tag{5}$$

where N is the number of elements in the employed data set.

The DNN model used in this work was implemented using Keras, a Python library (Anon, 0000). It has the following characteristics: the first layer has three units, which receive the information of the three color coordinates L*, a* and b*. Then, there are four hidden layers, each of which has 200 neurons. The activation function used in the output of each neuron is the rectified linear unit (Relu) (Nair and Hinton, 2010),

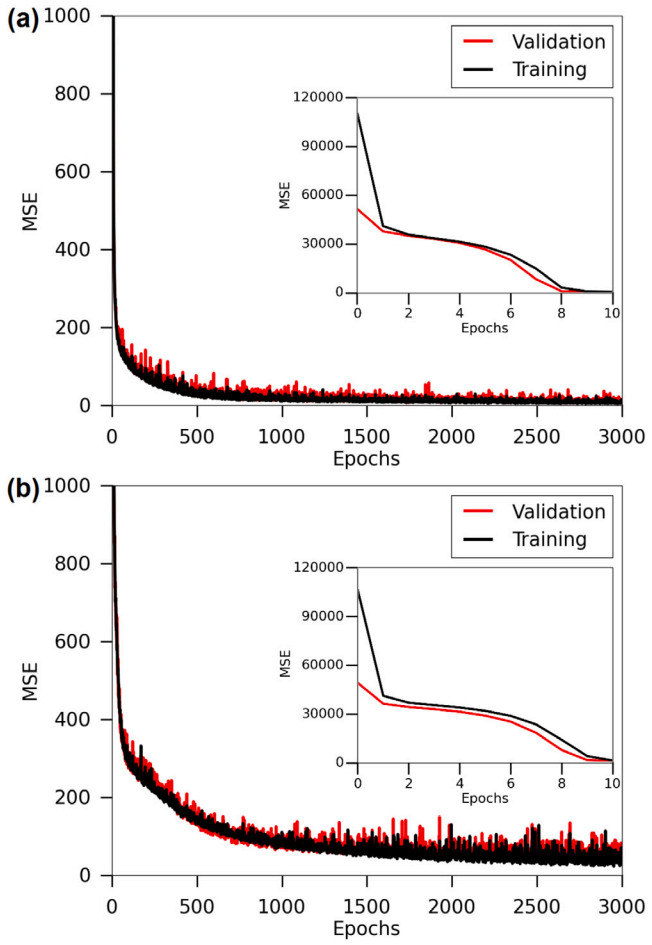

Fig. 5. MSE as a function of the number of epochs for the training and validation data, considering the databases of Fig. 3: (a) $R_2 = 130$ nm (Fig. 3(a)); (b) $R_2 = 190$ nm (Fig. 3(d)). The insets show the variation of the MSE for the first 10 epochs.

defined as $\sigma(x) = \max(0, x)$, which returns the value 0 for $x < 0$, and x for $x > 0$. Finally, the DNN has an output layer with two units, the values of R_1 and a. The weights are initialized using the Glorot uniform initialization (Glorot and Bengio, 2010) and the biases are set to zero, which is the default initialization in the Keras library. The number of epochs considered in the training and validation processes is 3000, and the optimization algorithm used to minimize the MSE is the Adam optimizer (Kingma and Ba, 2015).

In Fig. 5 we show the MSE as a function of the number of epochs for the training and validation data, for the color databases of Figs. 3(a) and 3(d). We divide the training and validation data into 24 and 3 subsets (batches), respectively. Since we consider 12000 training data and 1500 validation data in Fig. 5(a), the batch size, i.e., the number of elements in each subset, is 500. In Fig. 5(b) we consider 10080 training data and 1260 validation data, so that the batch size in this case is 420. It can be observed that, in both cases, the MSE value decreases as the number of epochs increases, which indicates that the DNN model is learning relationships between input and output variables. The training and validation processes are stopped in 3000 epochs because it was verified that the performance of the DNN does not improve further by increasing this number. After 3000 epochs, the training and validation curves in Fig. 5(a) reach MSE values of 7.1 and 8, respectively, whereas in the case of Fig. 5(b) the corresponding values are 30 and 23.

In the insets we show magnified versions of the leftmost parts of the graphs. It can be observed that the training and validation curves start with a very high MSE value, and both of them decrease rapidly in the first 10 epochs. Also, when comparing Figs. 5(a) and 5(b), it becomes evident that the learning process of the DNN is slower in this second case, i.e., for the database corresponding to $R_2 = 190$ nm. This behavior could be related to the fact that this database occupies a larger region in the color space.

The following step is the testing stage. It is important to remark that we build and train a DNN model to be able to retrieve the two geometrical parameters of the structure (R_1 and a) that can better reproduce a desired color. In order to evaluate the performance of the trained model, we calculate the difference between the target color and the color reflected by the optimized structure having the geometrical parameters predicted by the DNN. In the CIELAB color space, the distance between two colors, ΔE, whose color coordinates are (L_1*, a_1*, b_1*) and (L_2*, a_2*, b_2*), is defined as (McLaren, 1976):

$$\Delta E = \sqrt{(\Delta L)^2 + (\Delta a)^2 + (\Delta b)^2}, \tag{6}$$

where $\Delta L = L_1^* - L_2^*$, $\Delta a = a_1^* - a_2^*$ and $\Delta b = b_1^* - b_2^*$. It is important to mention that within the CIELAB color space, two colors are indistinguishable by the human eye if $\Delta E \leq 2.3$ (Mahy et al., 1994).

To illustrate the testing process, we consider the test data for the case $R_2 = 130$ nm: 1500 sets of the three CIELAB color coordinates and their associated geometrical parameters. In Fig. 6 we show the histogram of the distribution of ΔE for the test data obtained from the color database of Fig. 3(a). In the case under study, the condition $\Delta E \leq 2.3$ is met in approximately 83.5% of the test data (1253 colors), which means that these optimized colors are in very good agreement with the target ones. Complementary, $\Delta E > 2.3$ in 247 cases. To qualitatively assess the accuracy of the trained DNN for color reproduction, in the inset of Fig. 6 we include a comparison between the target and retrieved colors for 14 arbitrarily selected elements from the test data. We also indicate the retrieved values of R_1 and a and the value of ΔE. As observed, even for the highest value of ΔE (14.53), the target and the retrieved colors look very similar.

It is important to remark that, as stated above, there exist multiple structures in the database which display similar colors. Taking into account that we consider a random initialization of weights at the beginning of the training stage, different structures that produce the desired color could be found within the explored ranges of geometrical parameters. As a consequence, the present optimization model can find different structures, i.e., different pairs of values (R_1, a), for the same target color.

In the next section we illustrate the capability of the DNN model to predict the geometrical parameters of a structure that displays a given color determined by the three CIELAB color coordinates.

3.3. Prediction capability

To illustrate the prediction capability of the DNN model, we selected 10 arbitrary points in the CIELAB color space, which belong to the regions delimited by the databases considered in the examples of Fig. 4. Then, we applied the DNN model to retrieve the geometrical parameters of the layer of CS-MNPs that better produce these colors in reflection mode. In particular, in Figs. 7(a) and 7(b) we represent 10 points in the region occupied by the databases of Figs. 3(a) and 3(d), respectively. In the inserted tables, we include a comparison between the target and the retrieved colors for these selected points. For each color given by the L*, a* and b* color coordinates, the retrieved values of R_1 and a and the corresponding values of ΔE are also indicated. As observed, the optimized colors are in very good agreement with the target ones.

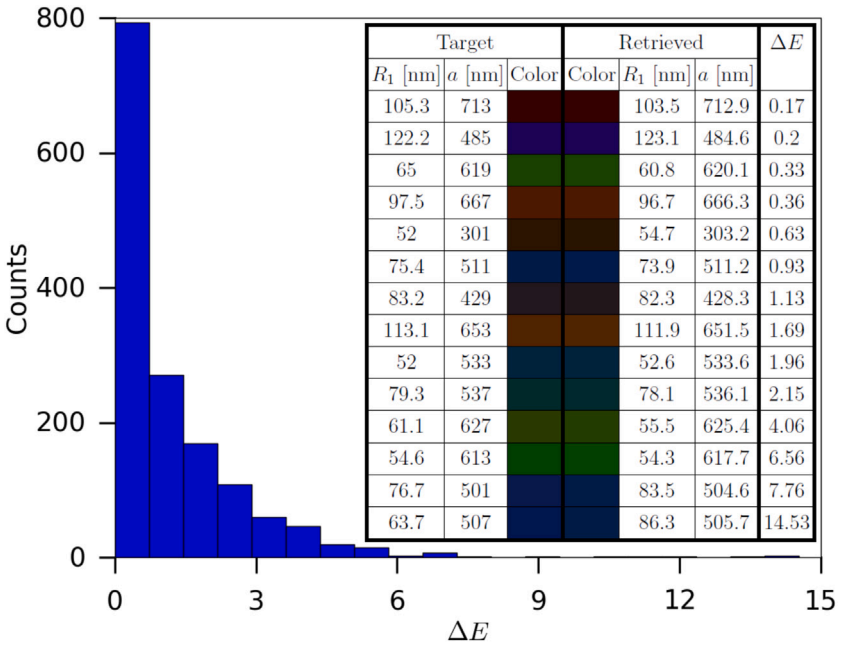

Target			Retrieved			ΔE
R_1 [nm]	a [nm]	Color	Color	R_1 [nm]	a [nm]	
105.3	713			103.5	712.9	0.17
122.2	485			123.1	484.6	0.2
65	619			60.8	620.1	0.33
97.5	667			96.7	666.3	0.36
52	301			54.7	303.2	0.63
75.4	511			73.9	511.2	0.93
83.2	429			82.3	428.3	1.13
113.1	653			111.9	651.5	1.69
52	533			52.6	533.6	1.96
79.3	537			78.1	536.1	2.15
61.1	627			55.5	625.4	4.06
54.6	613			54.3	617.7	6.56
76.7	501			83.5	504.6	7.76
63.7	507			86.3	505.7	14.53

Fig. 6. Histogram of the distance between the target and the predicted colors (ΔE). The inset shows a comparison between 14 target colors and their corresponding retrieved ones. The retrieved values of R_1 and a and the value of ΔE are also indicated. (For interpretation of the references to colour in this figure legend, the reader is referred to the web version of this article.)

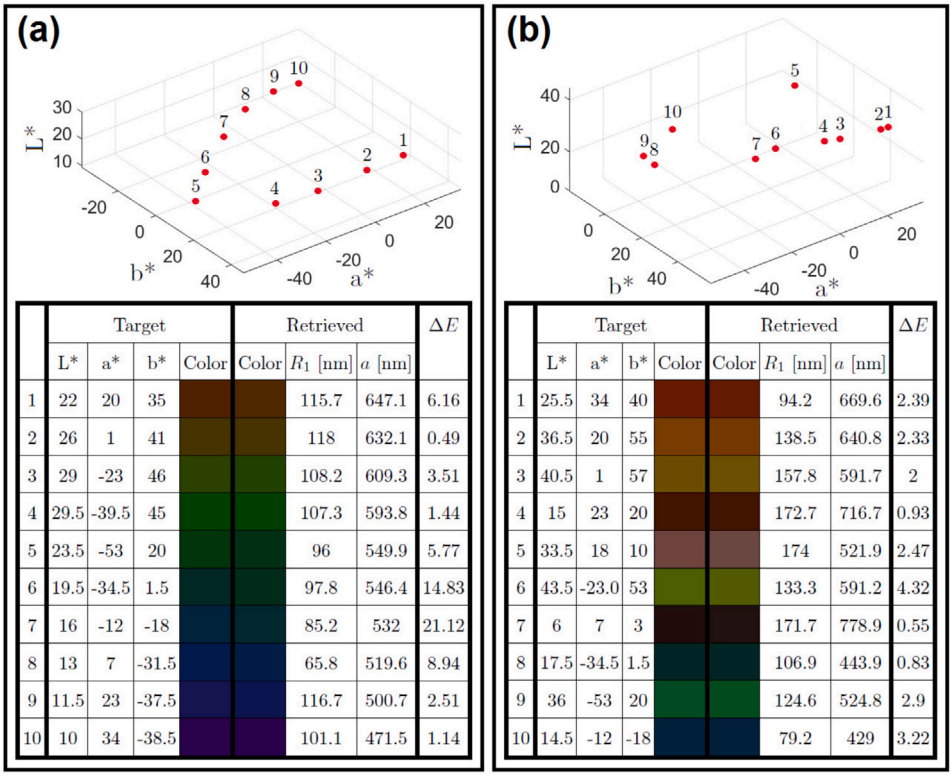

	Target				Retrieved			ΔE
	L*	a*	b*	Color	Color	R_1 [nm]	a [nm]	
1	22	20	35			115.7	647.1	6.16
2	26	1	41			118	632.1	0.49
3	29	-23	46			108.2	609.3	3.51
4	29.5	-39.5	45			107.3	593.8	1.44
5	23.5	-53	20			96	549.9	5.77
6	19.5	-34.5	1.5			97.8	546.4	14.83
7	16	-12	-18			85.2	532	21.12
8	13	7	-31.5			65.8	519.6	8.94
9	11.5	23	-37.5			116.7	500.7	2.51
10	10	34	-38.5			101.1	471.5	1.14

	Target				Retrieved			ΔE
	L*	a*	b*	Color	Color	R_1 [nm]	a [nm]	
1	25.5	34	40			94.2	669.6	2.39
2	36.5	20	55			138.5	640.8	2.33
3	40.5	1	57			157.8	591.7	2
4	15	23	20			172.7	716.7	0.93
5	33.5	18	10			174	521.9	2.47
6	43.5	-23.0	53			133.3	591.2	4.32
7	6	7	3			171.7	778.9	0.55
8	17.5	-34.5	1.5			106.9	443.9	0.83
9	36	-53	20			124.6	524.8	2.9
10	14.5	-12	-18			79.2	429	3.22

Fig. 7. CIELAB color coordinates of 10 arbitrarily selected colors within the regions of Fig. 4: (a) $R_2 = 130$ nm (Fig. 4(a)); (b) $R_2 = 190$ nm (Fig. 4(d)). A comparison between the target and retrieved colors, the retrieved values of R_1 and a, and ΔE are included.

4. Conclusions

In this work, a fully connected DNN was used to predict the relevant geometrical parameters of a layer of regularly arranged core–shell nanospheres that produce a desired specularly reflected color. The particles have a melanin core coated with silica, and the whole system is embedded in air. In order to design the DNN model, its relevant parameters and features were determined using a training and validation process, with the main objective of minimizing the difference between the target and the retrieved colors. To train, validate and test

the DNN we used a database formed by the geometrical parameters of the structure and the three CIELAB color coordinates, obtained from the specular reflectance simulated with the KKR method.

To evaluate the performance of the DNN model, we compared the distance, in the CIELAB color space, between the target color and the color produced by the retrieved structure. The inverse design strategy used in this work has proven to be successful in optimizing colors that have not been used for the training stage. It was found that the optimized colors are in very good agreement with the target ones, even in the case of colors arbitrarily chosen from the database region of the CIELAB color space.

Although we focused on a specific structure, the approach used in this work could be applied for the design of other artificial structures, such as 3D photonic crystals. The application of DNN models for color optimization could be useful for the design of materials with specific color properties.

Declaration of competing interest

The authors declare that they have no known competing financial interests or personal relationships that could have appeared to influence the work reported in this paper.

Funding

The authors acknowledge partial support from Universidad de Buenos Aires, Argentina (UBACyT 20020150100028BA and 20020190100108BA) and CONICET, Argentina (PIP 11220170100 633CO).

Data availability

No data was used for the research described in the article.

References

Anon, 0000. "Keras documentation https://keras.io/".

Baldi, P., 2021. Deep Learning in Science: Theory, Algorithms, and Applications. Cambridge University Press, Cambridge.

Baxter, J., Calà Lesina, A., Guay, J.-M., Weck, A., Berini, P., Ramunno, L., 2019. Plasmonic colours predicted by deep learning. Sci. Rep. 9 (1), 8074.

Dai, P., Wang, Y., Hu, Y., De Groot, C.H., Muskens, O., Duan, H., Huang, R., 2021. Accurate inverse design of Fabry–Perot-cavity-based color filters far beyond sRGB via a bidirectional artificial neural network. Photonics Res. 9 (5), B236–B246.

Dorado, L.A., Depine, R.A., Schinca, D., Lozano, G., Míguez, H., 2008. Experimental and theoretical analysis of the intensity of beams diffracted by three-dimensional photonic crystals. Phys. Rev. B 78, 075102.

Glorot, X., Bengio, Y., 2010. Understanding the difficulty of training deep feedforward neural networks. In: Proc. of the 13th International Conference on Artificial Intelligence and Statistics, Vol. 9. pp. 249—256.

González-Alcalde, A.K., Salas-Montiel, R., Mohamad, H., Morand, A., Blaize, S., Macías, D., 2018. Optimization of all-dielectric structures for color generation. Appl. Opt. 57, 3959–3967.

Goodfellow, I., Bengio, Y., Courville, A., 2016. Deep Learning. MIT Press.

Gralak, B., Tayeb, G., Enoch, S., 2001. Morpho butterflies wings color modeled with lamellar grating theory. Opt. Express 9, 567–578.

Huang, Z., Liu, X., Zang, J., 2019. The inverse design of structural color using machine learning. Nanoscale 11, 21748–21758.

Kingma, D.P., Ba, J.L., 2015. Adam: a method for stochastic optimization. In: Proc. of the 3rd International Conference on Learning Representations. pp. 1—15.

LeCun, Y., Bengio, Y., Hinton, G., 2015. Deep learning. Nature 521, 436–444.

Lozano, R., 1978. El Color y su Medición, Américalee Ed..

Ma, W., Liu, Z., Kudyshev, Z.A., Boltasseva, A., Cai, W., Liu, Y., 2021. Deep learning for the design of photonic structures. Nat. Photonics 15, 77–90.

Mahy, M., Van Eycken, L., Oosterlinck, A., 1994. Evaluation of uniform color spaces developed after the adoption of CIELAB, and CIELUV. Color Res. Appl. 19, 105—121.

Malkiel, I., Mrejen, M., Nagler, A., Arieli, U., Wolf, L., Suchowski, H., 2018. Plasmonic nanostructure design, and characterization via deep learning. Light: Sci. Appl 7 (1), 60.

McLaren, K., 1976. XIII–The development of the CIE 1976 (L*a*b*) uniform colour space and colour–difference formula. J. Soc. Dyers Colour 92 (9), 338–341.

Molesky, S., Lin, Z., Piggott, A.Y., Jin, W., Vucković, J., Rodriguez, A.W., 2018. Inverse design in nanophotonics. Nat. Photonics 12 (11), 659–670.

Nair, V., Hinton, G.E., 2010. Rectified linear units improve restricted Boltzmann machines. In: Proc. of the 27th International Conference on Machine Learning. pp. 807—814.

Peurifoy, J., Shen, Y., Jing, L., Yang, Y., Cano-Renteria, F., Delacy, B.G., Joannopoulos, J.D., Tegmark, M., Soljaĉić, M., 2018. Nanophotonic particle simulation and inverse design using artificial neural networks. Sci. Adv. 4 (6), eaar4206.

Pilozzi, L., Farrelly, F.A., Marcucci, G., Conti, C., 2018. Machine learning inverse problem for topological photonics. Commun. Phys. 1 (1), 57.

Rasamoelina, A.D., Adjailia, F., Sincak, P., 2020. A review of activation function for artificial neural network. In: Proc. of the IEEE 18th World Symposium on Applied Machine Intelligence and Informatics, Vol. 28. SAMI, pp. 281–286.

Sajedian, I., Badloe, T., Rho, J., 2019. Optimisation of colour generation from dielectric nanostructures using reinforcement learning. Opt. Express 27 (4), 5874–5883.

Stavenga, D.G., Leertouwer, H.L., Osorio, D.C., Wilts, B., 2015. High refractive index of melanin in shiny occipital feathers of a bird of paradise. Light: Sci. Appl. 4, e243.

Stefanou, N., Yannopapas, V., Modinos, A., 1998. Heterostructures of photonic crystals: frequency bands and transmission coefficients. Comput. Phys. Commun. 113, 49–77.

Stefanou, N., Yannopapas, V., Modinos, A., 2000. Multem 2: A new version of the program for transmission and bandstructure calculations of photonic crystals. Comput. Phys. Commun. 132, 189–196.

Xiao, M., Dhinojwala, A., Shawkey, M., 2014. Nanostructural basis of rainbow-like iridescence in common bronzewing, Phaps Chalcoptera feathers. Opt. Express 22 (12), 14625–14636.

Xiao, M., Hu, Z., Wang, Z., Li, Y., Tormo, A.D., Thomas, N.L., Wang, B., Gianneschi, N.C., Shawkey, M.D., Dhinojwala, A., 2017. Bioinspired bright noniridescent photonic melanin supraballs. Sci. Adv. 3 (9), e1701151.

Xiao, M., Li, Y., Allen, M.C., Deheyn, D.D., Yue, X., Zhao, J., Gianneschi, N.C., Shawkey, M.D., Dhinojwala, A., 2015. Bio-inspired structural colors produced via self-assembly of synthetic melanin nanoparticles. ACS Nano 9, 5454–5460.

Yannopapas, V., Modinos, A., Stefanou, N., 1999. Optical properties of metallodielectric photonic crystals. Phys. Rev. B 60 (8), 5359–5365.